The 2021 Loyalty Island earthquake (Mw 7.7): tsunami waveform inversion and implications for tsunami forecasting for New Zealand

Aditya Riadi Gusman, Jean Roger, William Power, and Bill Fry

GNS Science, Lower Hutt, New Zealand

(a.gusman@gns.cri.nz)

Key Points:

- Significant near trench slip on the plate interface of the 2021 Loyalty Island earthquake was estimated by inverting tsunami waveforms at coastal and offshore stations.
- Accurate tsunami forecast can be obtained from interpolating results of precomputed earthquake scenarios.
- The new New Zealand DART network is essential in improving the tsunami warning capability for countries in the South West Pacific.

Abstract

A tsunamigenic earthquake with thrust faulting mechanism occurred off the Loyalty Islands, New Caledonia, in the Southern New Hebrides subduction zone on the 10th of February 2021. The tsunami was observed at coastal gauges in the surrounding islands and in New Zealand. The tsunami was also recorded at a new DART network that was designed to enhance the tsunami forecasting capability of the Southwestern Pacific. We used the tsunami waveforms in an inversion to estimate the fault slip distribution. The estimated major slip

region is located near the trench with maximum slip amount of 4 m. The computed seismic moment for the source model of 3.39×10^{20} Nm (Mw 7.65) is slightly smaller than the Global Centroid Moment Tensor or USGS W-phase Moment Tensor solutions. We evaluate two tsunami forecasting approaches of selecting a pre-computed scenario and interpolating pre-computed scenarios for coastal regions in New Zealand. For the evaluation, we first computed the tsunami threat levels in New Zealand coastal regions from the earthquake source model to make a reference threat level map. The results show that the tsunami threat level maps from a pre-computed Mw 7.7 scenario located closest to the epicenter and from an interpolation of two scenarios matched the reference threat levels at most of the coastal regions. We also report on utilization of the coastal gauge and DART buoy data for updating forecasts in real-time during the event and discuss the differences between the rapid-response forecast and post-event retrospective forecasts.

Plain language summary

We estimated the tsunami source of the 2021 Loyalty Island earthquake from inversion of tsunami waveforms recorded at offshore DART and coastal stations. These DART stations are part of a new DART network that was designed to enhance the tsunami forecasting capability of New Zealand and the Southwestern Pacific region. The inversion result suggest that the earthquake ruptured the plate interface with relatively large slip near the trench. Our source model can explain the observed tsunami and its general slip distribution pattern is consistent with another independent earthquake source study from USGS that used teleseismic waveforms. The tsunami threat level map for New Zealand coastal regions produced from the source model is then used as a reference map to evaluate two techniques for rapid tsunami forecasting. Both techniques utilize pre-computed earthquake scenarios. The first technique is using the epicenter and magnitude of the earthquake to select the nearest earthquake scenario.

The second technique interpolates pre-computed results of two earthquake scenarios around the epicenter. The tsunami hindcast accuracies from the two techniques are high as the resulting tsunami threat levels matched the reference ones at most of the warning regions in New Zealand.

Keywords: Tsunami waveform inversion, the 2021 Loyalty Island earthquake, Southern New Hebrides/Vanuatu Subduction Zone, tsunami forecast, earthquake source model

1. Introduction

One of subduction zones in the Pacific Ocean that poses tsunami threats to New Zealand and other southwest Pacific states is the New Hebrides (also known as Vanuatu) subduction zone. In this region, thrust earthquakes occur on the plate interface between the subducting Australia plate and the overriding New Hebrides arc and North Fiji Basin (Calmant et al., 2003). On the 10th of February 2021, a magnitude (Mw) 7.7 earthquake occurred in this subduction zone and generated a tsunami (Figure 1). Based on the earthquake's magnitude, location and depth, a tsunami warning was issued by the Pacific Tsunami Warning Center (PTWC) for island nations around the epicenter in the South West Pacific such as New Caledonia, Fiji, Vanuatu, Tonga, New Zealand, and Australia. The National Emergency Management Agency (NEMA) of New Zealand issued tsunami threat warnings for several coastal regions in the country.

According to the United States Geological Survey (USGS), the earthquake occurred at 13:19:55 UTC with a hypocenter located at 23.054° S - 171.601° E and 10 km depth southeastward of the Loyalty Islands archipelago in the southern part of the New Hebrides subduction zone. It is located to the east of the region where the Loyalty Ridge, part of the Australian Plate, is subducted under the overriding Pacific Plate at a convergence rate of ~12 cm/yr and where Mw7.0+ tsunamigenic earthquakes occurred during the last century (Roger

et al., subm.). Since the May 17, 1995 Mw 7.7 Walpole tsunamigenic earthquake, the New Hebrides subduction zone, which is amongst the most seismically active, has produced at least 12 small (amplitude < 50 cm) to moderate (0.5 m < amplitude < 5 m) tsunamis. These tsunamis were triggered by earthquakes, such as the November 19, 2017 Mw 7.0 earthquake or the recent December 5, 2018 Mw 7.5 Tadine earthquake (Figure 1) whose maximum amplitude reached more than 2 m in New Caledonia and 4 m in Aneityum Island, Vanuatu (Sahal et al., 2010; Roger et al., 2019; Roger et al., 2021). Although the central and northern part of the New Hebrides subduction zone is also known to have experienced tsunamis triggered by even larger earthquakes of Mw 8.0+ (Ioualalen et al., 2017), there is no clear evidence for Mw8.0+ earthquakes in the southeasternmost part of the subduction zone (170°E-175°E), where the February 10, 2021 earthquake occurred. Lack of recorded large events may also have a physical explanation. In this region, the convergence is no longer eastward verging, as is the case for the rest of the subduction zone, but instead oriented N17°E perpendicular to the trench with a rate measured at ~5 cm/yr, making it the slowest converging part of the New Hebrides convergence zone (Calmant et al., 2003). For comparison, the subduction convergence rate north of 22°S is ~12 cm/yr.

The focal mechanisms provided by the Global Centroid Moment Tensor (GCMT) and USGS W-phase moment tensor (WMT) solutions suggest that the earthquake ruptured the plate interface with a nearly pure thrusting mechanism. The GCMT solution gives a seismic moment of 4.01×10^{20} Nm and nodal planes with strike = 279°/87°, dip = 23°/67°, and rake = 101°/85°. The USGS WMT solution gives a seismic moment of 4.36×10^{20} Nm and nodal planes with strike = 246°/92°, dip = 17°/75°, and rake = 65°/97°. The USGS finite fault model for the thrust faulting event maps earthquake rupture all the way to the trench with moment rate maximum at 15 s after earthquake origin time and rupture termination within 40 s.

97 This geometry of nearly pure thrusting earthquakes can trigger tsunamis with a main energy
98 axis orientation of South-Southwest/North-Northeast, i.e. toward New Zealand and
99 Southeastern Australia to the south and toward Vanuatu to the north (Okal, 1988). Thus, the
100 tsunami from the 2021 Loyalty Island earthquake propagated in the southwestern region of the
101 Pacific Ocean, and was recorded at local coastal gauges in New Caledonia and Vanuatu, and
102 also at regional distances in places like Fiji, Western Samoa, Tuvalu, Australia (including
103 Tasmania) and New Zealand, more than 3000 km away from the earthquake epicenter (Figure
104 1 and Figure 2 and Table 1). The tsunami was also recorded by the New Zealand network of
105 DART buoys in the Hikurangi-Kermadec-Tonga subduction zone (Figure 2)(Fry et al., 2020).
106 Deployment of this network was started by the government of New Zealand in December 2019
107 (DART NZA, B, C, E, and F) and September 2020 (DART NZG, H, and I) and is scheduled to
108 be finished in 2022 (DART NZD, J, K, and L) (Power et al., 2018). It was designed to enhance
109 the capability of New Zealand and other Pacific states to detect and forecast tsunamis in the
110 Southwestern Pacific and was strongly motivated by the recognized gap in operational response
111 to events occurring at regional propagation distances (Fry et al., 2018).
112 The procedures for tsunami early warning in New Zealand make use a two-stage approach
113 involving initial issuance of “action maps” and subsequent “threat maps”. The action maps are
114 based on highly uncertain early earthquake and magnitude estimates. They are designed to
115 rapidly and conservatively assess the possibility of land threat and trigger activation of
116 emergency response. They are binary maps, assigning “land threat” or “under assessment” to
117 coastal zones. This early forecast is based on pre-computed tsunami scenarios and simple 1D
118 tsunami prediction equations (Power, 2017). Following refinement of earthquake source
119 parameters, typically derived through available w-phase moment tensor inversions,
120 precomputed tsunami scenarios from earthquake sources located in subduction zones around
121 the Pacific Ocean are used to issue forecast maps. Forecast maps include tsunami amplitude

information. The precomputed tsunami scenario catalogue contains a total of ~1000 uniform fault slip models with earthquake magnitudes ranging from 6.9 to 9.3 (Gusman et al., 2019). A tsunami threat level map for coastal regions in New Zealand was prepared for every earthquake scenario. Pre-computed tsunami waveforms at coastal gauges and DART buoys are available too. In this database, there is a scenario available with the same magnitude and a location very close to the 2021 Loyalty Island earthquake.

Facing the enduring threat of tsunamis affecting their coastal populations and infrastructures, many countries have built tsunami pre-computed scenarios databases to support tsunami preparation and response, for example Japan (Tatehata, 1997; Hoshiba and Ozaki, 2014), French Polynesia (Reymond et al., 2012), Turkey (Onat and Yalciner, 2013), Australia (Greenslade et al., 2011), Indonesia (Harig et al., 2019), Portugal (Matias et al., 2012), New Caledonia (Duphil et al., 2021). High resolution tsunami inundation forecasting through scenario selection of pre-computed scenarios, or deep learning using pre-computed scenarios, have also been considered (Gusman et al., 2014; Mulia et al., 2018; Mulia et al., 2020). Ways to improve the use of those databases, and the accuracy of impact forecasting, especially for scenarios whose magnitude or location lie outside the ranges of the existing ones, are of major interest.

In this paper, the tsunami waveforms recorded at coastal gauges and DART stations are used in an inversion process to estimate the non-uniform fault slip distribution of the earthquake. The tsunami threat level map in New Zealand made from the earthquake source model was then used as a reference map (true state) to evaluate our tsunami forecasting approach. We compare the reference threat level map with the map for the nearest scenario with Mw 7.7 to the epicenter. We also evaluate a map created by interpolating the result from two Mw 7.7 scenarios around the epicenter. Here we describe the interpolation method to produce an interpolated threat level map and tsunami waveforms at observation points. Finally,

147 we discuss the effectiveness of the pre-computed scenarios for providing accurate tsunami
148 forecasts for New Zealand coastal regions. We conclude by describing response forecast
149 calibration based on data from coastal tide gauges and DART stations.

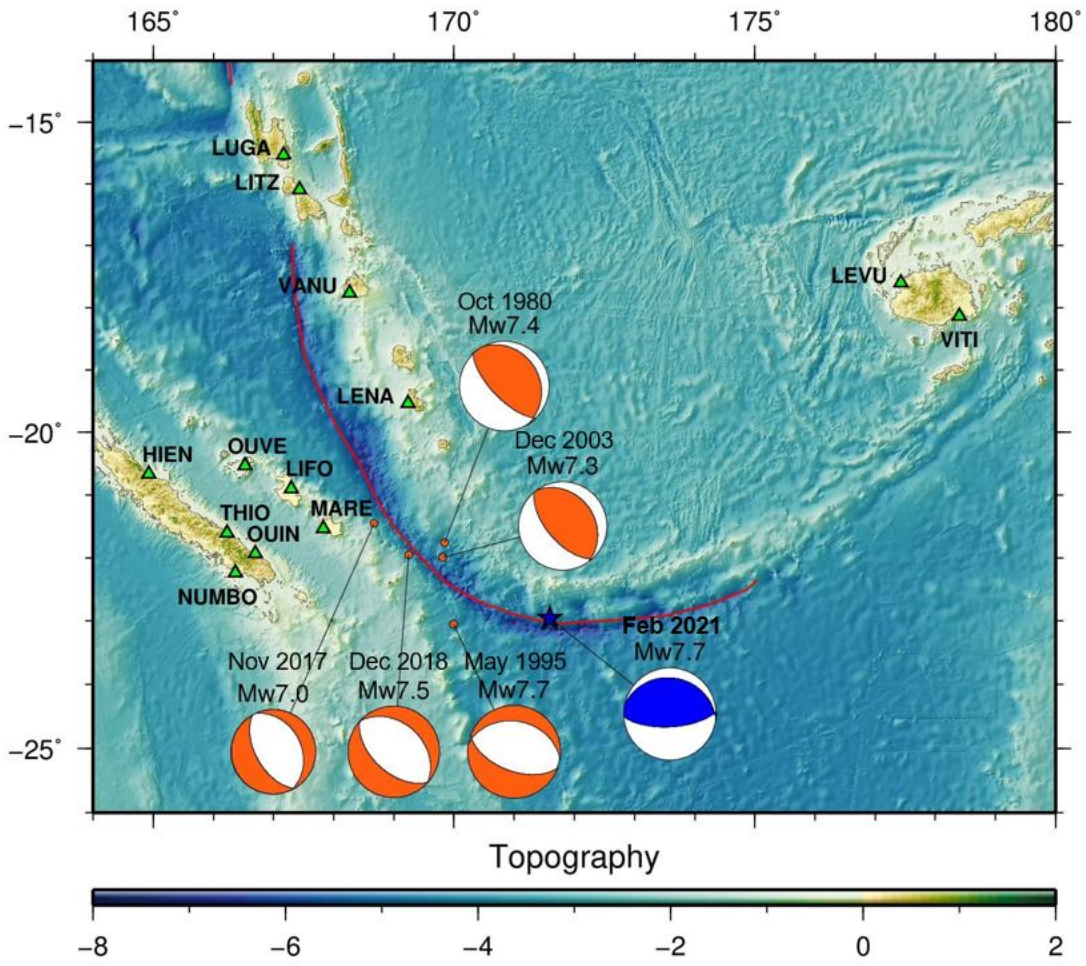

150

151

152 *Figure 1 Major tsunamigenic earthquakes in the New Hebrides subduction zone from 1980. Focal*
153 *mechanisms are based on GCMT solutions. Green triangles indicate coastal gauges at which the*
154 *tsunami waveforms used in this study were recorded. Convergent plate boundaries are indicated by red*
155 *lines.*

156

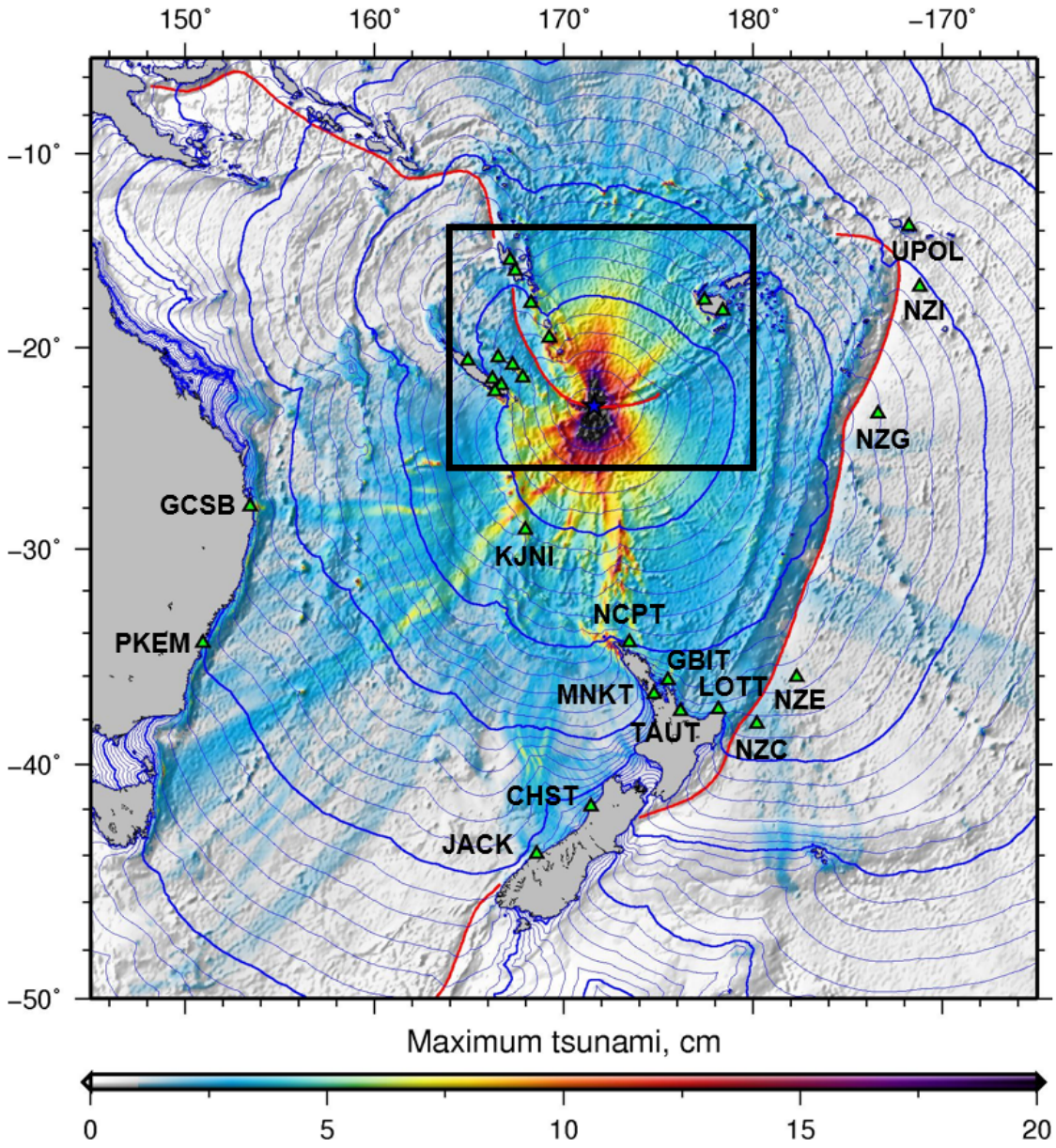

157

158 *Figure 2 Theoretical tsunami maximum amplitude and travel time from the epicenter calculated using*
159 *bathymetry data from the 2021 Loyalty Island earthquake source model. Thick blue contour lines*
160 *indicate time intervals of 1 hour, while thin blue contour lines indicate time intervals of 10 minutes.*
161 *Green triangles indicate coastal gauges and DART stations at which the tsunami waveforms used in*
162 *this study were recorded. Plate boundaries are indicated by red lines. Stations names for the green*
163 *triangles inside the black rectangle can be seen in Figure 1.*

164

2. Tsunami waveform and bathymetric data

2.1. Tsunami waveforms

The tsunami generated by the 2021 Loyalty Island earthquake was clearly recorded at coastal gauges in New Caledonia, Vanuatu, Fiji, Australia, Samoa, and New Zealand. The coastal gauge records were available from the IOC water level monitoring website (http://www.ioc-sealevelmonitoring.org). We removed the tides using a polynomial fit method to obtain the tsunami waveforms. The tsunami was also recorded at DART buoys NZC, NZE, NZG, and NZI which are located seaward of the Hikurangi-Kermadec-Tonga subduction zone trench (Figure 2). We also removed the tides recorded at the DARTs by the polynomial fit method. Then high frequency waves were removed using a low pass filter with cutoff period of 200 sec to get the tsunami waveforms.

Table 1. Coastal gauge and DART station information and the tsunami records sorted by distance from epicentre

Station Code	Location	Country/ Region	Longitude	Latitude	Distance from epicenter (km)	First wave amplitude (cm)	Travel time (minute)	Maximum amplitude (cm)
MARE	Maré	New Caledonia	167.8333	-21.5333	418	6.5	49	17.8
LENA	Lenakel	Vanuatu	169.2333	-19.5333	452	12.8	60	135.1
LIFO	Lifou	France	167.3000	-20.9000	498	16.6	68	36.6
OUIN	Ouinné	New Caledonia	166.7000	-21.9333	515	16.5	72	27.2
NUMBO	Nouméa	New Caledonia	166.3667	-22.2333	542	1.7	107.5	4.2
THIO	Thio	New Caledonia	166.2333	-21.6000	571	8.1	80	9.8
OUVE	Ouvéa	New Caledonia	166.5333	-20.5333	587	6.8	103	12.7
VANU	Port Vila	Vanuatu	168.2667	-17.7667	673	6.2	122	5.2
HIEN	Hienghène	New Caledonia	164.9333	-20.6667	732	4.1	101	9.5
KJNI	Norfolk Island	Australia	167.9667	-29.0667	769	11.4	88	43.6
LEVU	Lautoka	Fiji	177.4333	-17.6000	852	3.0	123	5.6
LITZ	Litzlitz	Vanuatu	167.4333	-16.1000	878	2.4	115	8.0
VITI	Suva	Fiji	178.4000	-18.1333	888	4.8	97	4.8
LUGA	Luganville	Vanuatu	167.1667	-15.5333	947	4.1	137	8.6
NCPT	North Cape	New Zealand	173.4667	-34.4333	1288	3.4	131	28.8

GBIT	Great Barrier	New Zealand	175.5000	-36.2000	1519	8.8	164	62.8
AUCT	Auckland	New Zealand	174.7667	-36.8333	1571	3.1	250	8.3
TAUT	Tauranga	New Zealand	176.1667	-37.6000	1684	1.3	189	3.9
LOTT	East Cape	New Zealand	178.1667	-37.5333	1737	6.2	164	23.9
GCSB	Gold Coast	Australia	153.4333	-27.9333	1902	20.5	240	30.5
UPOL	Apia	Samoa	188.2333	-13.8000	2026	1.4	223	4.2
CHST	Charleston	New Zealand	171.4333	-41.9000	2105	Not observable	Not observable	31.5
JACK	Jackson Bay	New Zealand	168.5667	-43.9667	2351	12.8	315	35.5
PKEM	Port Kembla	Australia	150.9333	-34.4667	2377	2.4	268	19.7
NZG	Kermadec	Kermadec	186.6000	-23.3667	1533	0.83	147	0.83
NZI	Kermadec	Kermadec	188.8000	-16.9000	1918	0.62	192.5	0.65
NZE	Hikurangi	Hikurangi	182.3000	-36.0333	1781	0.79	151.8	0.86
NZC	Hikurangi	Hikurangi	180.2000	-38.2000	1881	1.05	168.5	1.38

2.2. Bathymetric data and modelling grids

A nested grid configuration can be implemented in tsunami simulations to balance computational efficiency and numerical accuracy. There are two nested grid configurations used in this study. One is to simulate the synthetic waveforms for the inversion Green's functions, and the other one is used to calculate the tsunami threat levels in New Zealand.

For the synthetic tsunami waveforms simulation, we made a largest modelling domain that covers the nations in the South West Pacific Ocean around the earthquake source location with a grid size of 120 arc-sec. A set of nested modelling domains were made to focus on each of the coastal gauge with grid sizes of 40, 13.333, and 4.444 arc-sec. A combination of available bathymetric data with different coverage and grid size were used for the tsunami simulation. The highest resolution bathymetric data is always used to make each tsunami modelling grid. The GEBCO14 gridded bathymetric data with grid size of 30 arc-sec was used and resampled for the largest modelling domain and smaller domains in Australia and Fiji. A bathymetric grid with resolution of 100 m is available for the area around New Caledonia and Vanuatu. Higher resolution and quality bathymetric grids with resolution of 25 m are also available for the areas around coastal gauges in Maré (station code: MARE), Lifou (LIFO), Ouinné (OUIN), Thio

196 (THIO), Hienghène (HIEN), Lenakel (LENA), and Port Vila (VANU). For modeling grids
197 around New Zealand coastal gauges (AUCT, CHPT, GBIT, JACK, LOTT, MNKT, NCPT, and
198 TAUT), a high quality gridded bathymetric data with grid size of 10 arc-sec is available. The
199 complete coastal gauge information can be seen in Table 1.

200 For tsunami threat level map creation, a nested grid configuration with four modelling
201 domains was prepared. The largest modelling domain covers the whole Pacific Ocean with a
202 grid size of 4 arc-min. As the main purpose of this grid setup is for tsunami threat estimate in
203 New Zealand, other locations outside the country are only simulated using the coarsest
204 modelling grid. The next grid level of modelling domain covers the entire of New Zealand and
205 have grid sizes of 1 arc-min. The last grid level with finest grid size of 15 arc-seconds includes
206 two modelling domains that cover the two New Zealand's main islands and the Chatham
207 Islands.

208

209 ## 3. Tsunami waveform inversion

210 ### *3.1. Tsunami inversion method*

211 We first calculated two tsunami simulations using single fault models with fault
212 parameters from the GCMT and USGS W-phase MT solutions. The simulated tsunami
213 waveforms of these models are comparable. The trench is curved around the source area with
214 strike angles varying from 260° to 300° based on the USGS SLAB2.0 model (Hayes et al.,
215 2018). The trench-parallel strike angles according to USGS, GCMT and Geoscience Australia
216 are 246°, 279°, and 284° respectively. Because the strike angle from GCMT is at the middle of
217 these values, the strike of 279°, dip of 23°, and rake of 101° from the solution were assumed
218 for the fault parameters in the inversion as the strike angle from the solution is at the middle of
219 the other strike angle values (Figure 1). A fault with total length of 120 km and width of 60 km

was subdivided into 6 sub-faults along strike and 3 sub-faults down dip, resulting in a sub-fault size of 20 km by 20 km. The top edge of the shallowest sub-faults is located along the trench at depth of 1 km.

The seafloor displacement from each sub-fault was calculated using the Okada's formula (1985). These seafloor displacement models were used as the initial modelling conditions to simulate the tsunami waveforms. The linear long wave was simulated by solving the non-dispersive linear shallow water equations with a finite difference method and a staggered leap-frog scheme (Satake, 1995). Then a phase correction method (Watada et al., 2014; Gusman et al., 2015) was applied to the simulated linear long wave to include the dispersion effects due to the elasticity of the earth, seawater compressibility, and the gravitational potential variation. A unit slip amount of 1 m was used to construct the tsunami Green's functions. The tsunami amplitudes at some of the coastal gauges located near-field or far-field are about an order of magnitude larger than the amplitudes at DART buoys. To treat the coastal and deep ocean tsunami waveforms equally, we weight the DART data by 50. As fault slip must be smooth in some degree (Yabuki and Matsu'ura, 1992), a spatial smoothness constraint was incorporated by including a smoothing matrix consisting of a Laplacian operator. The Akaike's Bayesian Information Criterion (Akaike, 1980) was used to determine the optimal value of the smoothing factor. More details for the tsunami waveform inversion algorithm used in this study, which is based on the non-negative least square method (Lawson and Hanson, 1995) are available in previous studies (i.e., Gusman et al., 2010; Gusman et al., 2015).

3.2. Fault model resolution and quality

The The earthquake source area is surrounded by coastal gauges and DART buoys. To evaluate the source model resolution, we applied a checkerboard test (e.g., Lorito et al., 2010; Heidarzadeh and Gusman, 2021). The checkerboard pattern for the target model was made using slip amounts of 2 and 1 m (Figure 3). The target tsunami waveforms at the coastal gauges

and DART stations produced using this source model were degraded by adding Gaussian noise. We applied the tsunami inversion code with the target waveforms to get a slip distribution. We find that the checkerboard pattern on the shallower part of the fault can be well reproduced by the inversion, but not the pattern on the deepest part (Figure 3). This is because there is no nearby station located in the main path of the tsunami energy immediately north of the source.

To measure the uncertainty of the estimated slip distribution caused by various errors associated with tsunami modelling, we ran 30 tsunami waveforms inversions with different randomly selected tsunami waveform sets at 20 out of 28 stations. The uncertainty of the estimated slip distribution is represented by the standard deviation of these 30 slip distributions.

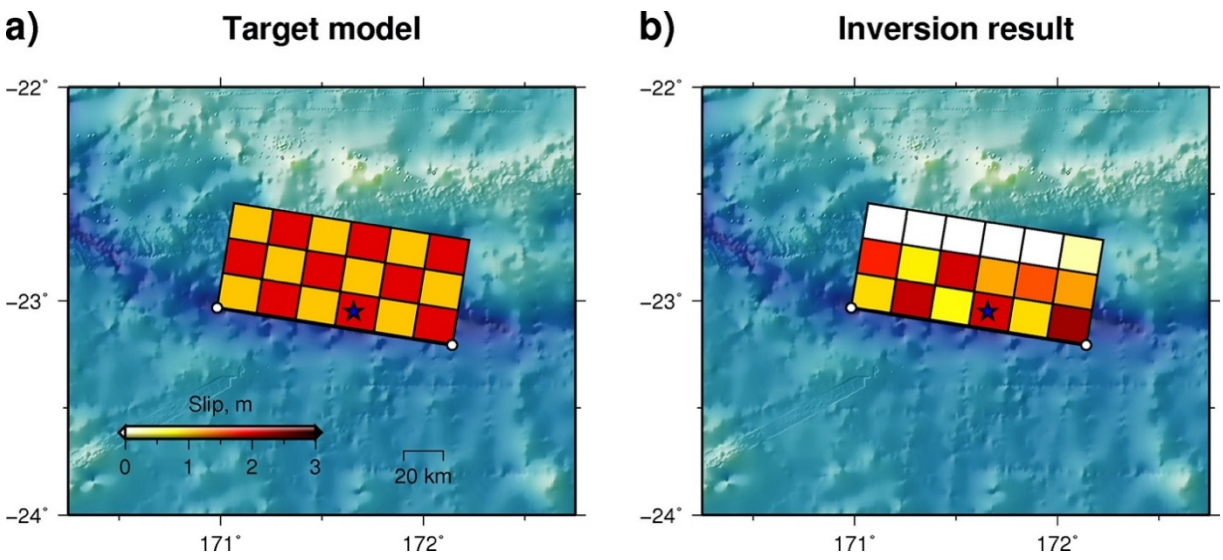

Figure 3 Checkerboard test result. a) Target slip distribution. b) Slip distribution obtained by an inversion using synthetic waveforms at the coastal gauges and DART stations generated from the target slip model. Slip amounts of 2 and 1 m were used to make the checkerboard pattern for the target slip model. The blue star represents the 2021 Loyalty Island earthquake epicentre.

3.3.The estimated slip distribution

An initial slip distribution estimated using only tsunami waveforms recorded at the coastal gauges is not so reliable as it has relatively large slip errors. It is sometime difficult to accurately simulate the tsunami amplitude and arrival time at coastal gauges especially without accurate bathymetric data. Some of the coastal gauges in Vanuatu, New Caledonia, and Fiji are located inside a bay or lagoon showing complex bathymetric features potentially leading to arrival time shifts, like shown for New Caledonia and Vanuatu by Roger et al. (2021). This problem of random arrival time shifts, which may be caused by instrumental clock problems, inaccurate station positions, bay effects, harbour effects, or unknown instrument responses, can be solved by applying optimum waveform time shifts in the inversion as demonstrated in previous studies (Romano et al., 2016; Ho et al., 2021).

Tsunami waveforms at DART stations can be used to help solve the problem of inaccurate simulated tsunami arrival time at coastal gauges. DART stations are located at the deep ocean thus accurate tsunami amplitude and arrival time can be simulated using the available global bathymetric dataset. We ran an inversion to get a slip distribution using only tsunami waveforms at the DART buoys. The simulated tsunami arrival times from this estimated slip distribution were then assumed to be very close to the actual ones. Thus, any arrival time delay could be attributed to factors other than the source location, and the simulated waveforms at the coastal gauges can be used as a reference for the time shift. We found the optimum tsunami time shift that minimized the waveform misfit at every coastal gauge manually. The time shift applied to the simulated waveforms at the coastal gauges were up to 5.5 minutes. The tsunami waveforms at these stations were shifted: MARE (3 min), OUIN (2.58 min), THIO (4.75 min), VANU (5.5 min), HIEN (3 min), NCPT (3 min), TAUT (4.6 min), and PKEM (3 min). The final slip distribution was obtained from tsunami waveforms at both coastal gauge and DART

stations with the optimum time shift applied to the coastal gauges based upon the simulated waveforms.

The estimated slip distribution has a major slip region near the trench (Figure 4a). This is consistent with the result from the USGS finite fault model (USGS, 2021) (Figure 4a). The maximum slip amount estimated in this study is 4.1 m (Figure 4a and Table 2). The estimated maximum uplift near the trench is 2.1 m while the subsidence is 0.24 m (Figure 4c and Figure 4d). The calculated seismic moment from the slip distribution, assuming a rigidity of 40 GPa (e.g., Fujii and Satake, 2008), is 3.39×10^{20} Nm or equal to Mw 7.65. This estimated seismic moment is close to the value (4.01×10^{20} Nm) from the GCMT solution. An inversion using only DART data which are relatively far away from the source gives a slightly smaller calculated seismic moment (3.05×10^{20} Nm). The use of data at near-field coastal gauge stations brings the estimated moment closer to the one from GCMT. Figure 5 shows that the estimated slip distribution results in tsunami waveforms that largely reproduce the observations at the coastal gauge and DART stations.

The uncertainty or error for the estimated slip distribution was calculated from the 30 inversions that were made with random combinations of stations. For the sub-fault with the largest slip (4.1 m), the error of the estimate is ±0.2 m or about 6% of the slip amount, which is very low. Higher error percentages for the sub-faults exist mainly on the eastern part of the fault model. The error distribution can be seen in Table 2 and Figure 4b. Overall, the reliability of the estimated major slip region is high with very low slip errors. This error estimate and also the checkerboard test result (Figure 3) show that the inversion result in the major slip region is well constrained and resolved by the station coverage.

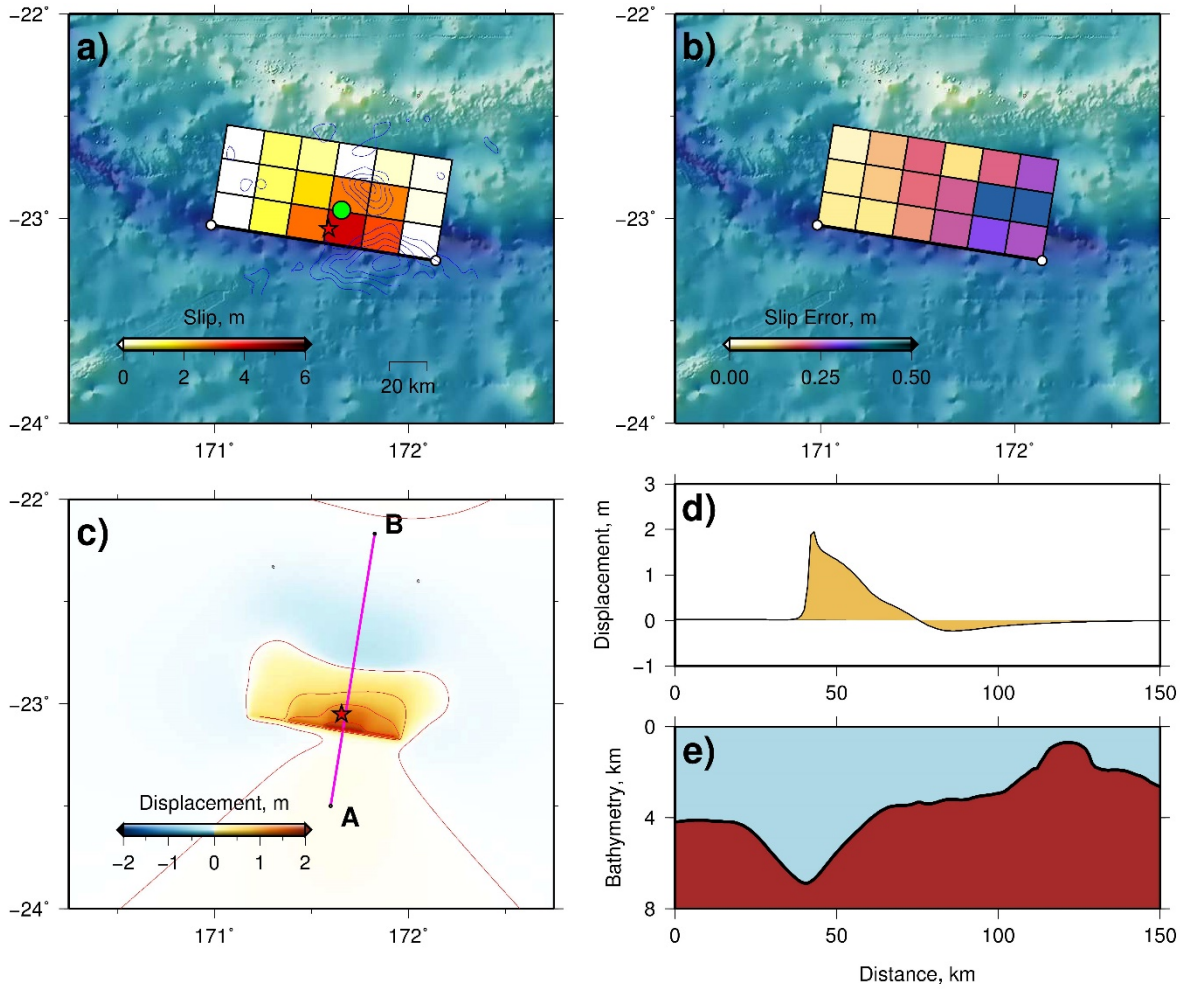

Figure 4 a) Slip distribution for the 2021 Loyalty Island earthquake estimated by tsunami waveform inversion using tsunami waveforms recorded at coastal gauges and DART stations. Blue lines represent the USGS finite fault model contours at 1 m intervals, the red star represents the epicentre and the green circle represents the GCMT centroid location. b) Slip error map for the estimated slip distribution. c) Calculated co-seismic seafloor vertical displacement from the estimated slip distribution. The vertical displacement contour interval is 0.5 m. The purple line indicates cross-section A-B. d) The estimated co-seismic seafloor vertical displacement profile along cross-section A-B. e) Bathymetric profile along cross-section A-B.

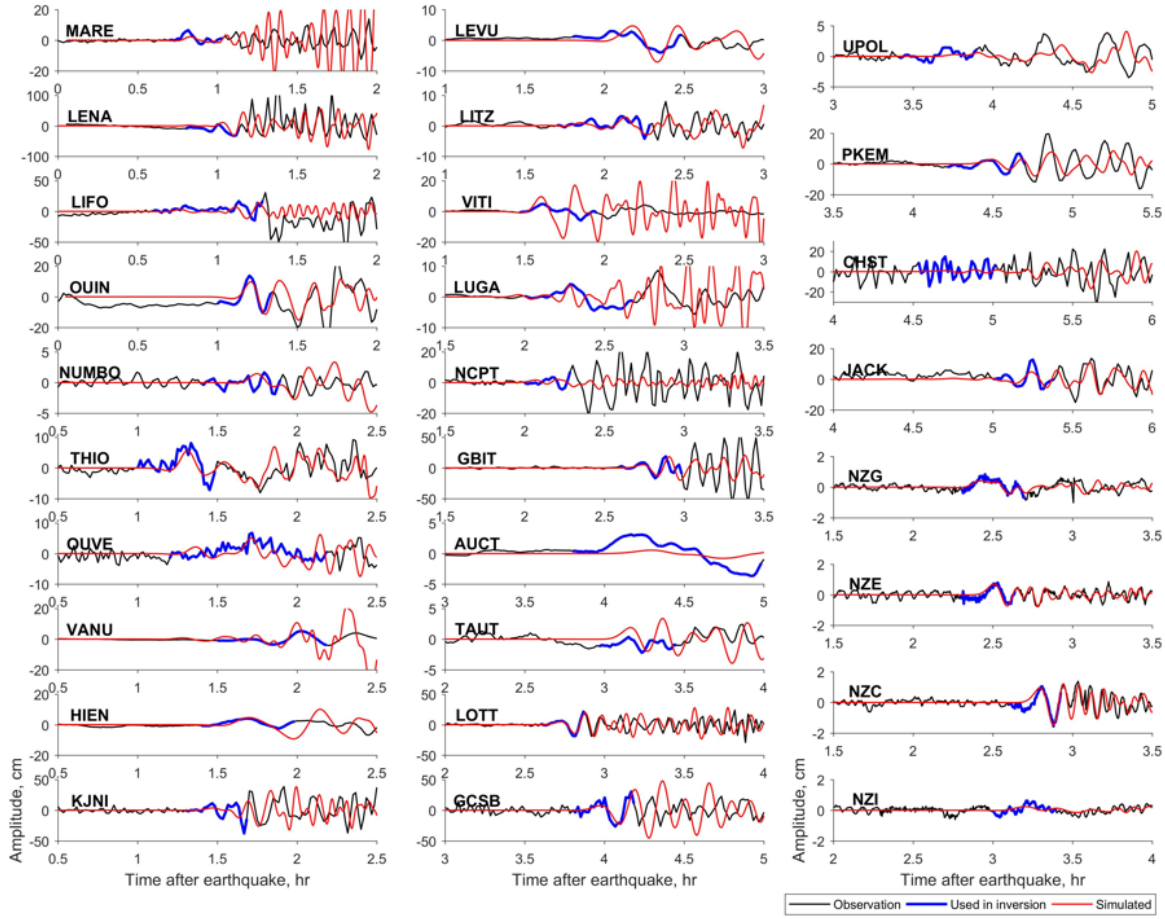

Figure 5 Comparison between the observed (black) and simulated (red) tsunami waveforms. Blue lines indicate the observed waveforms that were used in the inversion.

Table 2 Fault parameters and slip amounts from the tsunami waveform inversion

Lon (deg)	Lat (deg)	Length (km)	Width (km)	Depth (km)	Strike (deg)	Dip (deg)	Rake (deg)	Slip (m)	Error (±m)
172.1421	-23.2072	20	20	1	279	23	101	0	0.25
171.9489	-23.1783	20	20	1	279	23	101	3.12	0.29
171.7557	-23.1494	20	20	1	279	23	101	4.14	0.23
171.5625	-23.1206	20	20	1	279	23	101	2.8	0.16
171.3694	-23.0917	20	20	1	279	23	101	1.1	0.09
171.1762	-23.0628	20	20	1	279	23	101	0	0.08
172.1702	-23.0435	20	20	8.81	279	23	101	0.14	0.37
171.977	-23.0146	20	20	8.81	279	23	101	2.6	0.37
171.7838	-22.9858	20	20	8.81	279	23	101	2.71	0.22
171.5906	-22.9569	20	20	8.81	279	23	101	1.79	0.19
171.3974	-22.9281	20	20	8.81	279	23	101	0.92	0.13
171.2043	-22.8992	20	20	8.81	279	23	101	0	0.08
172.1983	-22.8799	20	20	16.63	279	23	101	0.09	0.26
172.0051	-22.851	20	20	16.63	279	23	101	0.31	0.21

171.8119	-22.8221	20	20	16.63	279	23	101	0.01	0.11
171.6187	-22.7933	20	20	16.63	279	23	101	0.61	0.2
171.4255	-22.7644	20	20	16.63	279	23	101	0.88	0.14
171.2323	-22.7355	20	20	16.63	279	23	101	0	0.05

4. Tsunami Forecasting for New Zealand

The COMCOT (Cornell Multi-Grid Coupled Tsunami model) program (Liu et al. 1998; Wang 2006; Wang and Power 2011) was used to make the database of tsunami threat level maps for New Zealand. The computer program was used to simulate tsunami generation and propagation from their sources to New Zealand coasts. A simulation time of 30 hours of tsunami propagation was used to ensure that maximum tsunami amplitudes were obtained. The nonlinear shallow water equations were solved to simulate the tsunami. Vertical wall boundaries were implemented by assuming any grid cell with an elevation larger or equal to -10 cm to be land.

The New Zealand coast is divided into 43 tsunami warning regions (NEMA 2020). There are six levels of tsunami threat in New Zealand, which are based on the coastal tsunami amplitude (Table 3). However, for tsunami warning dissemination, the threat levels are also grouped into three categories (Table 3), which are No Threat, Beach and Marine Threat, and Land and Marine Threat. For each earthquake scenario, the 99^{th} percentile of all coastal tsunami amplitudes within each warning region is calculated and then used to identify the tsunami threat level. The value for the 99^{th} percentile is used instead of the maximum value to avoid outliers.

Table 3 Tsunami threat levels in New Zealand with their tsunami height thresholds, colour codes, descriptions and threat level names for dissemination.

Threat Level	Tsunami Amplitude	Colour	Description	Threat level for dissemination
0	$h \leq 0.3$ m	White	No threat	No threat
1	$0.3 < h \leq 1$ m	Green	Threat to beach and small boats	Beach and Marine threat
2	$1 < h \leq 3$ m	Light blue	Some land threat	Land and Marine threat
3	$3 < h \leq 5$ m	Blue	Moderate land threat	
4	$5 < h \leq 8$ m	Pink	High land threat	
5	$h > 8$ m	Purple	Severe land threat	

4.1. Tsunami threat levels from the estimated fault slip distribution

The tsunami simulation from the estimated fault slip distribution categorizes many tsunami warning regions as being under Beach and Marine Threat, and no region is under the Land and Marine Threat. The warning regions that should be under the Beach and Marine Threat according to that source include the West Coast of the North Island from Cape Reinga to Kaipara Harbour, and from Mokau to Hawera; the East Coast of the North Island from Cape Reinga to Waihi Beach excluding the East Coast of Auckland, and from Matata to Mahia; and the West Coast of the South Island from Farewell Spit to Milford Sound (Figure 6a). The other coastal regions are under No Threat. However, it should be noted that the procedure described here for determining the tsunami threat levels from an estimated source model is challenging during an event. The complexity of tsunami waveform inversion and the many hours required for simulating the tsunami on high resolution grids using the source model are the main drawbacks. Real-time operationalisation of an inversion-based forecasting approach can be improved with simplification of the problem including possibilities of more coarsely defining the finite fault earthquake model and using empirical coastal amplitude equations to approximate

370 coastal threat zones. In this study, the threat level map from the estimated source model is
371 used purely as reference to evaluate the forecast based on the pre-computed scenarios.
372 During the response, the New Zealand Tsunami Expert Panel (NZTEP) used a coarse
373 simplification to adjust forecasts, described further in section 5.3.

374 The amplitude of the first observed tsunami wave cycle can be much smaller than the
375 maximum observed tsunami amplitude at coastal gauges. As an example, the amplitude of
376 the first wave at NCPT (North Cape) station is only 4 cm while the maximum amplitude
377 recorded by the same station is 29 cm. The complete list of the observed first wave cycle
378 amplitudes and the maximum amplitudes at the stations can be seen in Table 1. This
379 emphasises that the simulation time should be set long enough to capture the maximum
380 simulated tsunami amplitude.

381 Several coastal zones in the South Island are identified by this method as being under
382 the Beach and Marine Threat with tsunami larger than 0.3 m. The observed first tsunami
383 wave cycle amplitude in Jackson Bay which is located in the West Coast region of South
384 Island is 13 cm, while the maximum amplitude is 35 cm which validates the tsunami threat
385 level from the estimated fault slip distribution. Both simulation and observation at Jackson
386 Bay show that the tsunami is even higher than in some of the stations in the North Island.
387 Bathymetric features, and especially the Challenger Plateau and Bellona Basin (Figure 7b)
388 (Uruski, 2010), allow the tsunami to focus part of its energy on the West Coast of the South
389 Island as shown by the snapshots of the tsunami propagation shown in Figure 7a and the
390 maximum tsunami amplitude distribution in Figure 7c. The part of the tsunami propagating
391 over the deeper Bellona Basin goes with a faster speed than the part propagating over the
392 neighbouring shallower Challenger Plateau: the tsunami front slows down when arriving
393 on the northwesternmost part of the Challenger Plateau, wrapping around the set of
394 seamounts in the area around 38°S, 167°E (Rowden et al., 2005) and concentrating the

energy at the back of the seamounts, with a trajectory still oriented toward the West Coast of the South Island but with higher amplitudes. In addition, numerous submarine canyon complexes located along the southwestern margin of the Challenger Plateau (Neil et al., 2015) act as waveguides to focus tsunami waves on specific locations and can also explain the higher waves recorded at Jackson Bay (Figure 7d).

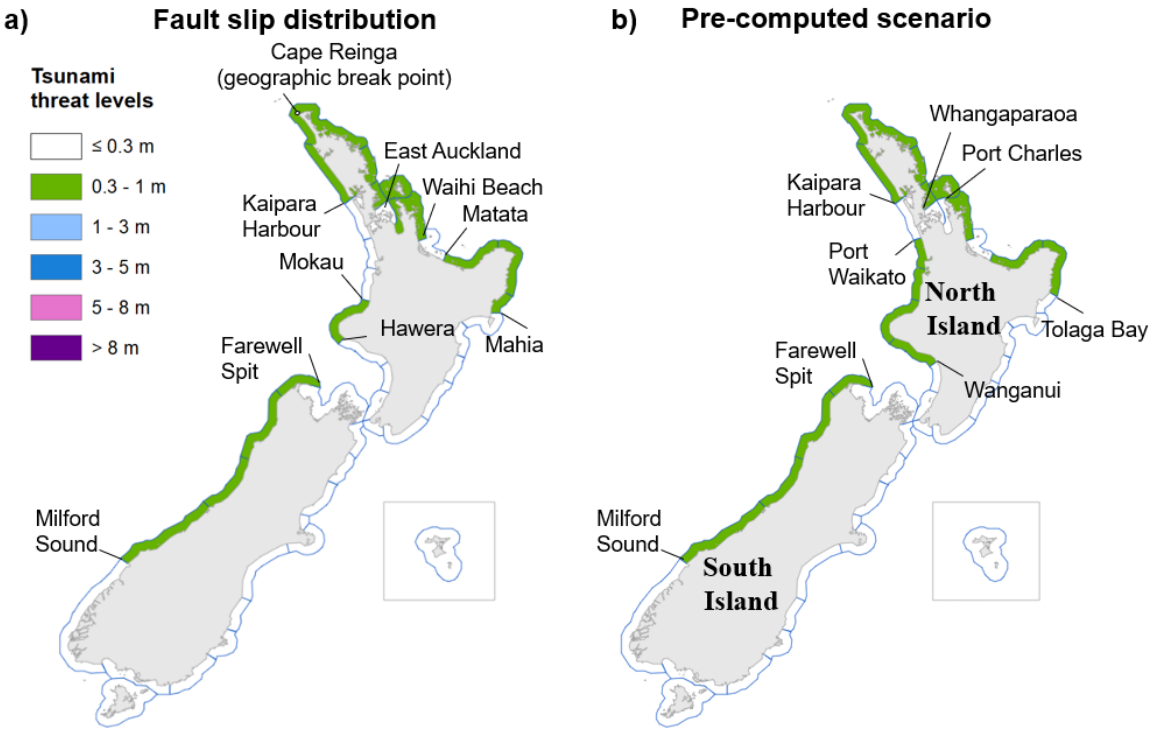

Figure 6 Tsunami threat level maps for New Zealand from a) a computation using the estimated fault slip distribution of the 2021 Loyalty Island earthquake and b) a pre-computed earthquake scenario (Mw 7.7) that best matches the epicentre and magnitude of the earthquake.

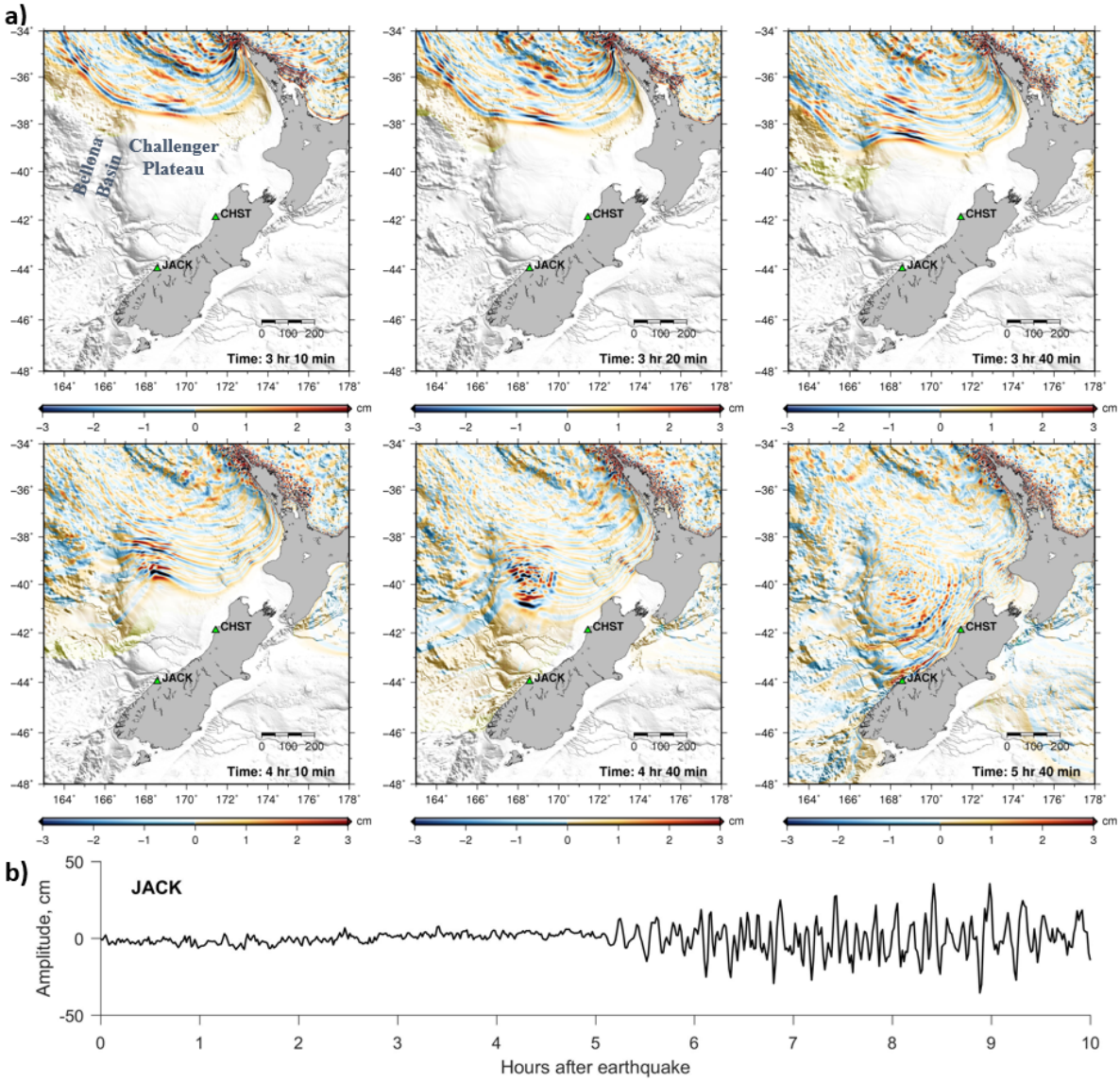

406

407

408

409 *Figure 7 a) Simulated tsunami propagation snapshots from the 2021 Loyalty Island earthquake source model over Bellona*
410 *Basin and Challenger Plateau near New Zealand. Green triangles indicate the locations of JACK and CHST coastal gauges. b)*
411 *Observed tsunami waveforms at JACK (Jackson Bay) coastal gauge.*

412

413 ### *4.2. Tsunami threat levels from a nearest pre-computed scenario*

414 Earthquake scenarios in subduction zones around the Pacific Ocean were used to build
415 a database of tsunami threat level in New Zealand. The size of the fault patches used for
416 the earthquake scenarios in the New Hebrides subduction zone is 50 km long and 25 km

417 wide. The earthquake scenario moment magnitudes (Mw) are ranged from 6.9 to 9.3, with
418 magnitude interval of 0.2. The distance between the scenario's epicentres for magnitudes
419 7.5, 7.7, and 7.9 is 150 km. The assumed fault parameters and orientations for the fault
420 models in this region are based on fault patches developed by the U.S. National Oceanic
421 and Atmospheric Administration (NOAA) (Gica et al., 2008) and those available from
422 Power et al. (2012). An earthquake scenario in the New Hebrides subduction zone with a
423 moment magnitude of 7.7 that is the nearest to the 2021 Loyalty Island earthquake epicentre
424 was selected from the database. This scenario epicentre is ~70 km westward the actual
425 epicentre. The uniform slip earthquake scenario has four fault patches and a slip amount of
426 2.2 m.

427 The predicted threat levels at most of the coastal regions (38 out of 43 regions) matched
428 the reference ones (Figure 6). Just like the threat level map from the fault slip distribution,
429 the one from the pre-computed scenario has no warning region that should be under the
430 Land and Marine Threat (Figure 6b). The warning regions that should be under the Beach
431 and Marine Threat include the West Coast of the North Island from Cape Reinga to Kaipara
432 Harbour, and from Port Waikato to Wanganui; the East Coast of the North Island from
433 Cape Reinga to Waihi Beach excluding the region from Whangaparaoa to Port Charles,
434 and from Matata to Tolaga Bay (Figure 6b). While the threat levels for the warning regions
435 in the South Island from the two models are the same. The selected scenario underestimated
436 the tsunami threat in two warning regions by one level lower and overestimated the threat
437 in three warning regions by one level higher.

438

439 *4.3. Interpolated tsunami threat levels from pre-computed scenarios*

440 The tsunami from the earthquake can be approximated by interpolating simulation
441 results from scenarios located around the epicentre (e.g., Tatehata, 1998). Here we

interpolated the threat level maps from these two scenarios with the inverse distance weighting method (Shepard, 1968). A general way of finding an interpolated tsunami threat level (f_i) in the 43 warning regions (i = 1, 2, …, 43) for a given epicentre based on pre-computed tsunami threat level in the database $f_{i,j}$ for j = 1, 2, …, Ns is to use the following equation:

$$f_i = \begin{cases} \frac{\sum_{j=1}^{Ns} w_j \cdot f_{i,j}}{\sum_{j=1}^{Ns} w_j}, if\ d \neq 0 for\ all\ j, \\ f_{i,j}, if\ d = 0\ for\ some\ j, \end{cases}$$

Eq. (1)

where

$$w_j = \frac{1}{d^p}$$

Eq. (2)

, d being the distance between the earthquake epicentre and scenario epicentre (reference point), Ns the number of scenarios which is 2 in this case, and p the power parameter set to 1.

As mentioned above, the reference point or epicentre of the selected scenario is westward the actual epicentre. We produced a threat level map by interpolating the tsunami heights in the warning zones from the selected nearest scenario with Mw7.7 located west of the epicentre (West Mw7.7 described in 4.2) and the second nearest scenario with also Mw7.7 located east of the epicentre (East Mw7.7). The vertical displacements and maximum tsunami amplitude distributions from these two scenarios can be seen in Figure 8. The interpolation result shows that there is one warning region which is the North Cape area from Ahipara to Bay of Islands (Figure 9a) that should be under the Land and Marine

Threat, while there is no region under this threat category from the previous two models. The warning region from Waihi beach to Matata should be under No Threat according to the reference map (Figure 6a), which is a level lower than the one according to the interpolation result (Figure 9a). While the threat levels for the other warning regions are the same as those in the selected scenario.

The interpolated threat levels (Figure 9a) at most of the coastal regions (36 out of 43 regions) matched the reference ones (Figure 6a). Based on the reference threat level map, the selected scenario underestimated the tsunami threat in two warning regions by one level lower and overestimated the threat in five warning regions by one level higher. This makes the forecast accuracy from the interpolation result slightly worse than the one from the selected scenario nearest to the epicentre. The interpolated threat levels are overall slightly higher than the one from the selected nearest scenario. The overestimated warning levels are because the earthquake source model that was used for to make the reference map has a slightly smaller seismic moment ($Mo = 3.39 \times 10^{20}$ Nm equivalent to moment magnitude Mw7.65) than the pre-computed scenario one (Mw7.7).

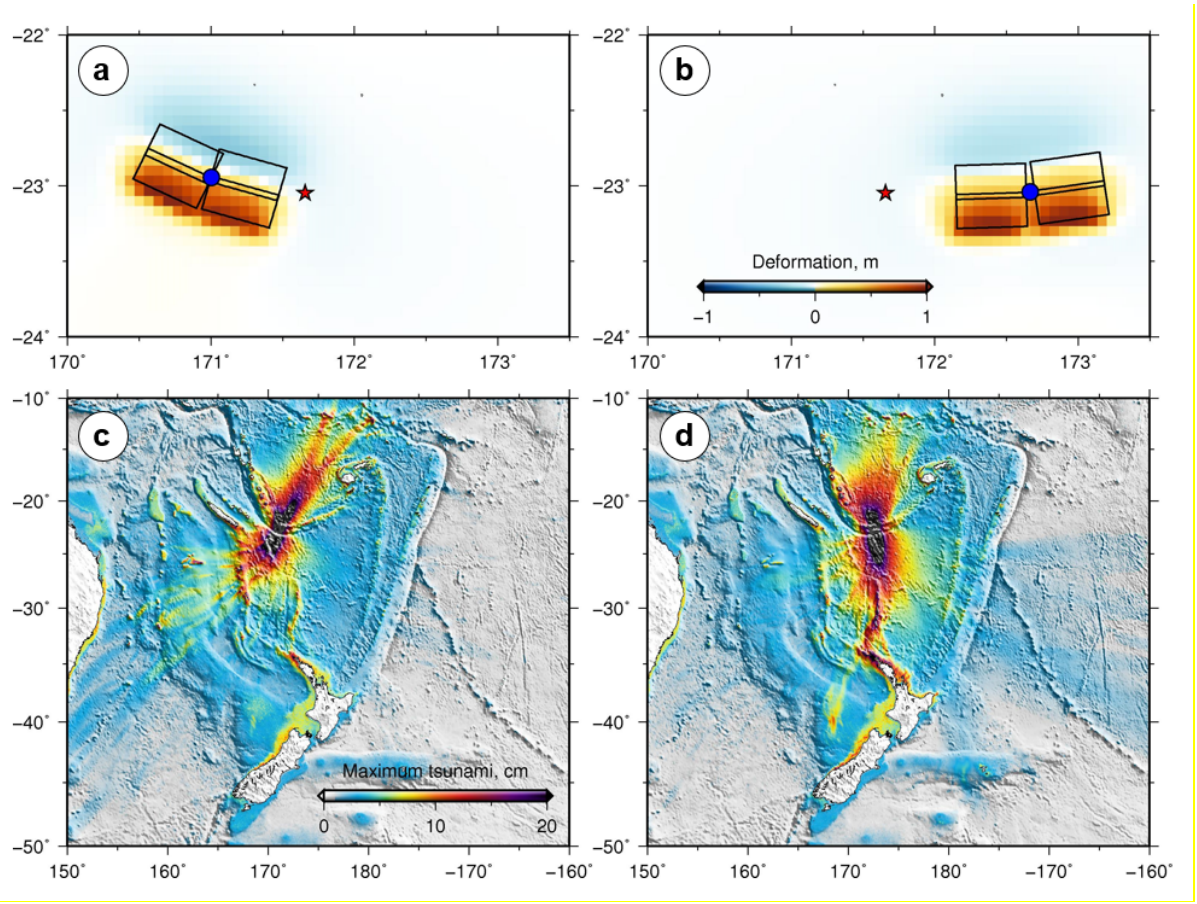

480

481 *Figure 8. Initial tsunami simulation of seafloor displacements and simulated tsunami amplitude distributions for the (a and*
482 *c) WestMw7.7 uniform slip scenario (nearest scenario) and (b and d) EastMw7.7 uniform slip scenario. Black rectangles*
483 *indicate the fault patches used by the scenario. The blue star represents the earthquake epicentre, while the blue dot*
484 *represents the reference point/epicentre for the scenario.*

485

486

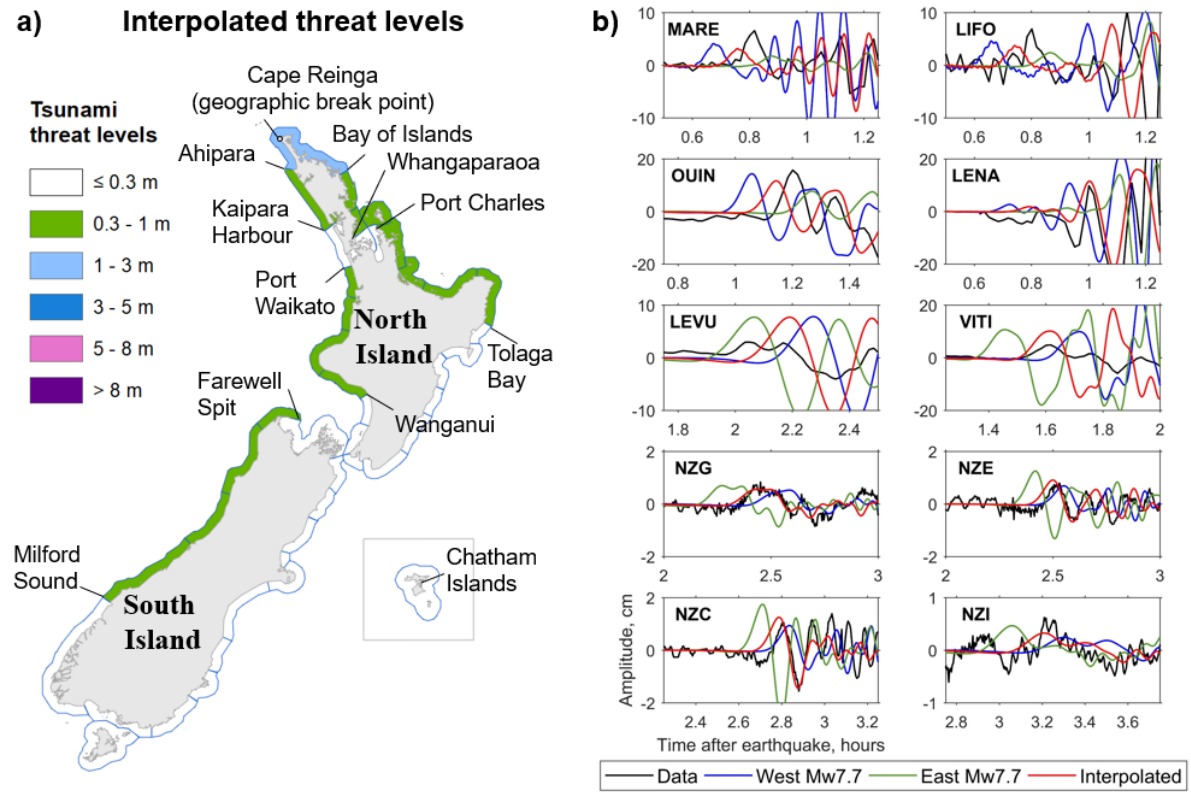

Figure 9 a) Threat level map obtained by interpolating the results from two Mw7.7 scenarios nearest to the epicentre. b) Observed, simulated and interpolated tsunami waveforms. Red lines indicate the interpolated tsunami waveforms from tsunami waveforms of the selected nearest scenario Mw7.7 located west of the epicentre (blue lines) and those of a second nearest scenario Mw7.7 located east of the epicentre (green lines). The locations of the scenarios are shown in Figure 8a and b.

5. Discussion

5.1. Toward improved real-time update of tsunami threat level maps

The tsunami forecast using pre-computed scenario database approach may not be enough if it only relies on the earthquake magnitude estimate. Tsunami records at coastal gauges and DART stations can be used to confirm or update the tsunami threat level. For this event, the tsunami arrived in the North Cape of New Zealand approximately 2 hours after the earthquake. Within 1.5 hours after the earthquake, at least one complete tsunami wave cycle had been recorded at four coastal gauges (MARE, OUIN, LIFO, and LENA) located in the azimuthal quadrant west-northwest of the epicentre. The sea level recorded

503 within 2 hours after the earthquake at LEVU and VITI which are located in Fiji to the east
504 of the epicentre can be used to evaluate the tsunami. While the tsunami arrival times at the
505 two closest DART stations (NZG and NZE) are approximately 2.5 hours after the
506 earthquake. We note that planned network expansion will provide 3 additional DART
507 stations within one-hour travel time of this earthquake source. When complete, the array is
508 designed to detect events originating from any Hikurangi/Kermadec/Tonga/New Hebrides
509 trench source within 30 minutes. Any warning update for this event based on the currently
510 operational DART stations would be too late for first wave arrival at North Cape but could
511 be valuable prior to maximum wave arrivals and also for dynamic forecasting during the
512 latter stages of the threat, supporting staggered de-escalation. This shows that the already
513 planned additional DART stations (Power et al., 2018) need to be deployed around the New
514 Hebrides subduction zone to enable a rapid characterization of any tsunami generated in
515 this area that threaten New Zealand and the nearby islands.

516 The existing pre-computed tsunami waveforms at coastal gauges outside New Zealand
517 were simulated using a low-resolution modelling grid (4 arc-min) as explained in Section
518 2.2. To make the observed tsunami waveform at coastal gauges more useful in validating
519 or updating a tsunami warning, the pre-computed tsunami waveforms need to be obtained
520 using high resolution grids. In this study we simulated the tsunamis at coastal gauges with
521 our highest modelling grid resolution for the two uniform slip scenarios (West Mw 7.7 and
522 East Mw 7.7) located around the actual epicentre (Figure 8a and b).

523 The tsunami waveforms from these two scenarios can be interpolated to get the
524 estimated tsunami waveforms for the event (Figure 9b). We used a waveform interpolation
525 method (Wang et al., 2019) which is based on the Huygens-Fresnel principle. Equations
526 Eq. (1) and Eq. (2) can be modified and then used to interpolate the tsunami arrival times
527 and amplitudes for an interpolated event. First, we estimated the arrival time at the stations

for the interpolated event. The interpolated arrival time at k[th] station of t_k^{arr} is calculated from the simulated arrival time from the scenarios $t_{k,j}^{arr}$ using the following equation:

$$t_k^{arr} = \frac{\sum_{j=1}^{Ns} w_j \cdot t_{k,j}^{arr}}{\sum_{j=1}^{Ns} w_j}$$

Eq. (3)

The simulated arrival time of each scenario is marked when the amplitude of the simulated tsunami at the station reached a threshold. The thresholds for coastal gauges are >1 cm while that for DARTs is 0.1 cm. Then the tsunami waveforms (y_k) can be interpolated from the amplitudes of the two simulated waveforms ($Y_{k,j}$) using the following equation:

$$y_k(t - t_k^{arr}) = \frac{\sum_{j=1}^{Ns} w_j \cdot Y_{k,j}\left(t - t_{k,j}^{arr}\right)}{\sum_{j=1}^{Ns} w_j}$$

Eq. (4)

The interpolated tsunami waveforms fit better the observations in term of both amplitude and arrival time compared to those from the two nearest Mw7.7 scenarios as shown in Figure 9b. At coastal gauges located west of the epicentre such as MARE, LIFO, OUIN and LENA, the West Mw7.7 scenario tsunami arrived earlier than the observation, and the East Mw7.7 scenario tsunami arrived after the observed arrival time. At station located east of the epicentre such as LEVU and VITI coastal gauges and the DARTs, the East Mw7.7 scenario tsunami arrived earlier than the observation, and the West Mw7.7 scenario tsunami arrived after the observed arrival time. While the interpolated waveforms arrived almost at the same time as the observations. To evaluate the scenarios the tsunami waveforms misfits are calculated. The data-simulation misfit is defined as $\sum \frac{|\max(d) - \max(s)|^2}{|\max(d)||\max(s)|}$, where d and s are the peak amplitudes of the first wave cycle of the observed and simulated tsunami waveforms, respectively. The amplitude data-simulation misfit for the interpolated (misfit = 15.7) and WestMw7.7 (misfit = 16.2) tsunami

551 waveforms are very similar, and these values are much smaller than 25.3 from EastMw7.7
552 scenario (Figure 10). Some selected waveforms used to calculate these misfits can be seen
553 in Figure 9b.

554 In retrospect, after the earthquake moment magnitude became available, we had two
555 tsunami threat level maps. One was from the scenario nearest to the epicentre and the other
556 was an interpolated threat level map from two scenarios nearest to the epicentre. To make
557 a conservative tsunami forecast, the higher threat level at each warning zone from the two
558 scenarios should be selected. The tsunami waveforms recorded within 1.5 hours at the
559 nearby four coastal gauges showed that the interpolated scenario have tsunami waveforms
560 with better tsunami arrival time but slightly worse tsunami amplitude predictions
561 ($misfit_{1.5hours}$ = 1.09) compared to those from the nearest scenario to the epicentre
562 ($misfit_{1.5hours}$ = 0.42) (Figure 10). The analysis with more tsunami waveforms at DART
563 stations and coastal gauges that were available more than 2.2 hours after the earthquake
564 suggest that the best scenario was the interpolated scenario which has a smaller misfit
565 (Figure 10) and better tsunami arrival time prediction.

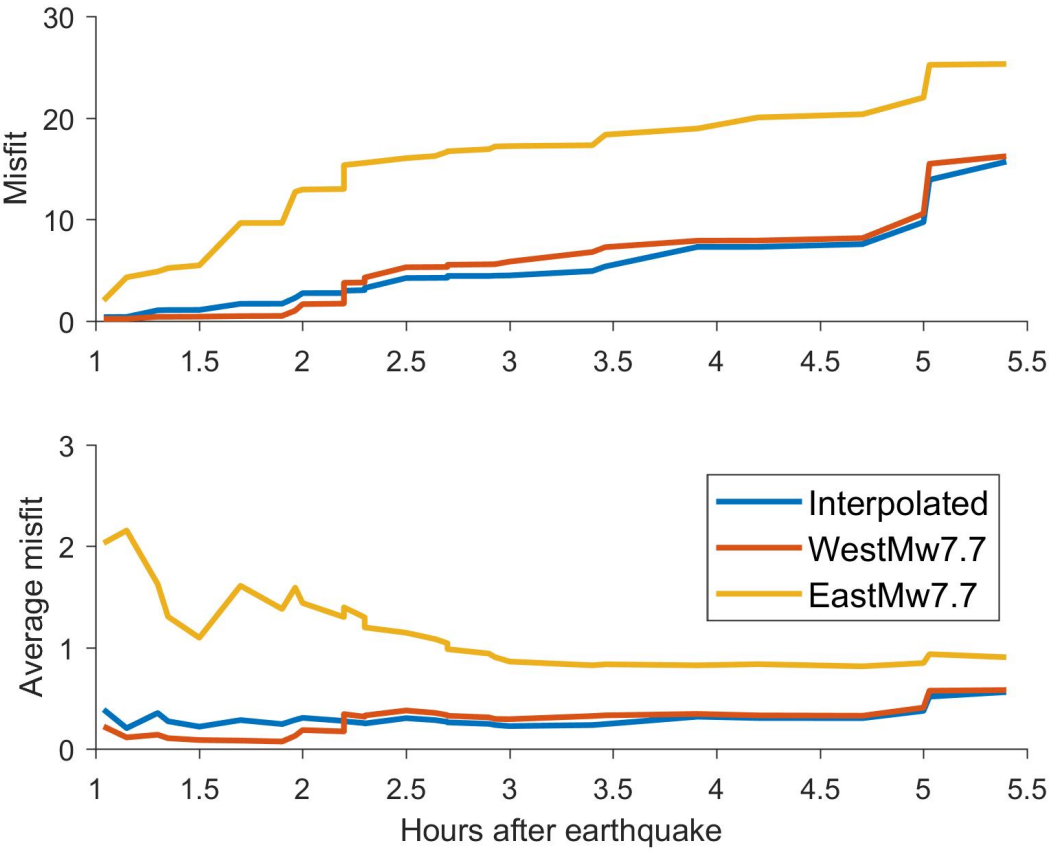

566

567 *Figure 10 Misfit and average misfit of tsunami amplitude at observation stations from the interpolated, WestMw7.7,*
568 *EastMw7.7 scenarios. The misfit is increasing over time as the number of stations used for the calculation increases. The*
569 *average misfit is the misfit divided by the number of stations.*

570

571 ### *5.2. Expanding the scenario database*

572 The current tsunami threat level maps for New Zealand are all based on thrust
573 earthquake scenarios. The 2021 Loyalty Island earthquake was also a thrust event. The
574 magnitude and focal mechanism of the earthquake can be confidently concluded in about
575 2 hours before the tsunami reaches any New Zealand coastline or 30 minutes after the
576 earthquake occurred. However, initial earthquake magnitude estimates for unusual kinds
577 of tsunamigenic earthquakes such as tsunami earthquakes (Kanamori, 1972) may not be
578 accurately obtained as quickly as those of typical thrust faulting earthquakes. Tsunami
579 earthquake scenarios may be further developed by assuming a rigidity of 10 GPa which is
580 smaller than the currently used one of 40 GPa when calculating the slip amount from any

given moment magnitude. It has been shown that the use of smaller rigidity for tsunami earthquakes with a given moment magnitude provides better tsunami impact predictions (Tanioka et al., 2017).

Large tsunamigenic intraplate earthquakes with the potential to create disastrous tsunamis may also occur with normal faulting mechanisms, such as the 1933 Sanriku (Mw 8.4), 1977 Sumba (Mw 8.3), and 2017 Chiapas (Mw8.2) earthquakes (Lynnes and Lay, 1988; Tanioka and Satake, 1996; Gusman et al., 2009; Gusman et al., 2018; Melgar et al., 2018). There is currently no scenario in the database with normal faulting mechanism, thus an update that includes this earthquake mechanism is recommended.

As shown above, if the current pre-computed scenario were used to forecast the tsunami in the near field, the actual tsunami arrived after the predicted arrival time in New Caledonia, while the tsunami arrived before the predicted arrival time in Fiji. This is because the selected scenario is Westward the actual epicentre and the distance between scenarios is 150 km. Also, the plate boundary is curved around the earthquake source and the strike angles of fault model patches there varies from 260° to 300°. These suggest that the earthquake scenarios around the source region are not dense enough for those two countries. A simple rule for the distance between the scenarios based on the earthquake magnitude may be applied to expand the scenarios. The distance can be set to be at least half of the typical fault length for a given earthquake magnitude. This will give scenario distance of 50 km for earthquake scenarios with magnitudes from 7.5 to 7.9. Interpolation between scenarios may be more effective than having more scenarios and would be computationally more efficient to try to cover every possible earthquake that might occur. Although adding more scenarios is preferred for areas like the Southern New Hebrides subduction zone that have fault patches with a significant range (>20°) of strike angles.

606 *5.3. Rapid Response*

607 In real-time, the response relied on threat-level maps derived from precalculated
608 scenarios as described above. The NZTEP used modelling based on a coarse simplification
609 of the earthquake source to validate the pre-calculated models. These simplified models
610 used 50 km × 100 km subduction zone unit sources and precalculated wave propagation
611 Green's Functions from the propDB database accessed within the ComMIT software
612 (Titov et al., 2011). One unit source (NV37b centered at 22.69° S – 171.55° E) was used
613 to represent the earthquake rupture with homogeneous slip. Based on a seismic magnitude
614 of Mw7.7, initial response simulations calculated the tsunami wavefield resulting from 2m
615 slip. The resulting forecasts were used to augment the threat maps based on the pre-
616 calculated scenarios described above. During the response, it was noted that forecast
617 amplitudes were less than those recorded at coastal tide gauges and DARTs. To account
618 for this discrepancy, a precautionary approach was taken and the modelled slip was
619 adjusted to ~4m, increasing the estimated earthquake magnitude to Mw7.9. This is
620 compatible with the maximum slip amount of 4.1 m as described above. The pragmatic
621 effect of this adjustment was to inform the expect duration of the Marine and Beach threat.
622 We note that manual calibration of the forecast is an interim step toward real-time
623 inversion based forecasting. Current and future work is aimed at implementing inversion
624 of DART data and improved forecasting. The Loyalty Island earthquake and tsunami
625 represent a valuable datapoint to help characterize the uncertainties involved in coarse
626 discretization of the earthquake source and determine an acceptable tradeoff between
627 computational time and forecast accuracy.

628

6. Conclusions

We estimated the slip distribution of the 2021 Loyalty Islands earthquake from tsunami waveforms recorded at 4 DART stations and 24 coastal gauges. The tsunami threat levels in coastal regions in New Zealand from the estimated slip distribution are then used as a reference map to evaluate the performance of our pre-computed earthquake scenario database selection and interpolation approaches for tsunami forecasting. The main results are:

i) The major slip region of the estimated fault slip distribution is located near the trench with maximum slip amount of 4.1 m. The computed seismic moment for the source model of 3.39×10^{20} Nm (Mw7.65) is consistent with the Global Centroid Moment Tensor and USGS W-phase Moment Tensor solutions.

ii) The coastal gauge records clearly showed that the largest amplitudes may be observed many hours after the tsunami arrived and the oscillation may last for more than 10 hours after the earthquake. Therefore, long tsunami simulation time is needed to properly calculate the potential tsunami threat from an earthquake scenario, for our scenarios the simulation time is 30 hours.

iii) The threat level of coastal regions in the West Coast of South Island of New Zealand is the same as some of those in the North Island even though the two locations are as far as 1000 km apart. The tsunami simulation results suggest that the tsunami was refracted by the Challenger Plateau and Bellona Basin which refocused some of its energy towards the West Coast of South Island.

iv) A tsunami threat level map can be obtained by interpolating two nearest Mw 7.7 earthquake scenarios (WestMw7.7 and EastMw7.7) to the epicentre available in the database. In this case the tsunami waveforms recorded at the coastal gauges and DART stations show that the interpolated waveforms matched the observed tsunami amplitude and arrival time better than those from the two Mw 7.7 in the

database. However, threat level validation or update from the analysis of tsunami data must be done with caution especially if the station azimuthal coverage is still poor during an event. The azimuthal coverage can increase as the tsunami propagates and is recorded by more stations.

v) The threat level maps from the nearest scenario and the interpolation both give accurate tsunami forecast for most warning zones. For a conservative forecast an ensemble tsunami threat level map can be obtained from the two maps. In this case the ensemble tsunami forecast is the same as the interpolation result.

vi) The existing earthquake scenarios are not dense enough to accurately forecast the tsunami in countries near the epicentre such as New Caledonia, Vanuatu and Fiji. A solution for this problem is by densifying earthquake scenarios. Another option with much lower computational cost is by interpolating the threat levels and tsunami waveforms from the existing available scenarios.

7. Acknowledgements

We thank Maxime Duphil (IRD, Nouméa, New Caledonia) for providing us with the bathymetric grid around some of the coastal gauges in New Caledonia. We thank David Burbidge from GNS Science, New Zealand for reviewing our manuscript. Funding for parts of this work was provided by the New Zealand Rapid Characterisation of Earthquakes and Tsunami programme. DART data available on request from the authors or New Zealand's GeoNet (www.geonet.org.nz). Tide gauge data available from the Intergovernmental Oceanographic Commission of UNESCO (IOC) (http://www.ioc-sealevelmonitoring.org/). Figures in the main text were made by GMT (https://www.generic-mapping-tools.org) and MATLAB (www.mathworks.com) software.

679 ## 8. References

680

681 Calmant S., Pelletier B., Bevis M., Taylor F., Lebellegard P., and Phillips, D. (2003). New
682 insights on the tectonics of the New Hebrides subduction zone based on GPS results, J.
683 Geophys. Res., 108, B6, 2319-2340, 2003.

684 Duphil, M., Aucan, J., Lefèvre, J., Pelletier, B., Roger, J., Thomas, B. (2021). Tsunami hazard
685 assessment in New Caledonia. TsuInfo Alert, 23(1),
686 https://www.dnr.wa.gov/publications/ger_tsuinfo_2021_v23_no1.pdf.

687 Fry, B.; Gledhill, K.R.; Benites, R.A. (2018). Ground motions in New Zealand from Kermadec
688 megathrust earthquakes. Lower Hutt, N.Z.: GNS Science. GNS Science report 2018/33. 17
689 p.; doi: 10.21420/7J43-G338

690 Fry, B.; McCurrach, S.-J.; Gledhill, K.R.; Power, W.L.; Williams, M.; Angove, M.; Arcas, D.;
691 Moore, C. (2020). Sensor network warns of stealth tsunamis. *Eos, 101:* doi:
692 10.1029/2020EO144274

693 Fujii, Y., & Satake, K. (2008). Tsunami sources of the November 2006 and January 2007 great
694 Kuril earthquakes. Bulletin of the Seismological Society of America, 98(3), 1559-1571.

695 Gica, Edison. "Development of the forecast propagation database for NOAA's Short-term
696 Inundation Forecast for Tsunamis (SIFT)." (2008).

697 Greenslade, D., Allen, S.C.R., Simanjuntak, M.A. (2011). An evaluation of tsunami forecasts
698 from the T2 scenario database. Pure and Applied Geophysics, 168, 1137-1151,
699 https://doi.org/10.1007/s00024-010-0229-3.

700 Gusman, A. R., Tanioka, Y., Matsumoto, H., & Iwasaki, S. I. (2009). Analysis of the Tsunami
701 Generated by the Great 1977 Sumba Earthquake that Occurred in IndonesiaAnalysis of the
702 Tsunami Generated by the Great 1977 Sumba Earthquake that Occurred in Indonesia.
703 Bulletin of the Seismological Society of America, 99(4), 2169-2179.

Gusman, A. R., Tanioka, Y., Kobayashi, T., Latief, H., & Pandoe, W. (2010). Slip distribution of the 2007 Bengkulu earthquake inferred from tsunami waveforms and InSAR data. Journal of Geophysical Research: Solid Earth, 115(B12).

Gusman, A. R., Tanioka, Y., MacInnes, B. T., & Tsushima, H. (2014). A methodology for near- field tsunami inundation forecasting: Application to the 2011 Tohoku tsunami. Journal of Geophysical Research: Solid Earth, 119(11), 8186-8206.

Gusman, A. R., Murotani, S., Satake, K., Heidarzadeh, M., Gunawan, E., Watada, S., & Schurr, B. (2015). Fault slip distribution of the 2014 Iquique, Chile, earthquake estimated from ocean- wide tsunami waveforms and GPS data. Geophysical Research Letters, 42(4), 1053-1060.

Gusman, A. R., Mulia, I. E., & Satake, K. (2018). Optimum sea surface displacement and fault slip distribution of the 2017 Tehuantepec earthquake (Mw 8.2) in Mexico estimated from tsunami waveforms. Geophysical Research Letters, 45(2), 646-653.

Gusman, A.R.; Lukovic, B.; Peng, B. (2020). Tsunami threat level database update: regional sources and tsunami warning text. Lower Hutt, N.Z.: GNS Science. GNS Science report 2019/83. 57 p.; doi: 10.21420/PTDC-NS18

Harig, S., Immerz, A., Weniza, Griffin, J., Weber, B., Babeyko, A., rakowsky, N., Hartanto, D., Nurokhim, A., Handayani, T., Weber, R. (2019). The tsunami scenario database of the Indonesia Tsunami Early Warning System (InaTEWS): evolution of the coverage and the involved modeling approaches. Pure and Applied Geophysics, 177, 1379-1401, https://doi.org/10.1007/s00024-019-02305-1.

Hayes, G. P., Moore, G. L., Portner, D. E., Hearne, M., Flamme, H., Furtney, M., & Smoczyk, G. M. (2018). Slab2, a comprehensive subduction zone geometry model. Science, 362(6410), 58-61.

728 Heidarzadeh, M., & Gusman, A. R. (2021). Source modeling and spectral analysis of the Crete
729 tsunami of 2nd May 2020 along the Hellenic Subduction Zone, offshore Greece. *Earth,*
730 *Planets and Space*, *73*(1), 1-16.
731 Ho, T. C., Satake, K., Watada, S., & Fujii, Y. (2019). Source estimate for the 1960 Chile
732 earthquake from joint inversion of geodetic and transoceanic tsunami data. Journal of
733 Geophysical Research: Solid Earth, 124(3), 2812-2828.
734 Hoshiba, M., & Ozaki, T. (2014). Earthquake Early Warning and Tsunami Warning of the
735 Japan Meteorological Agency, and Their Performance in the 2011 off the Pacific Coast of
736 Tohoku Earthquake Mw 9.0). In *Early warning for geological disasters* (pp. 1-28). Springer,
737 Berlin, Heidelberg.
738 Ioualalen, M., Pelletier, B., & Gordillo, G. S. (2017). Investigating the March 28th 1875 and
739 the September 20th 1920 earthquakes/tsunamis of the Southern Vanuatu arc, offshore
740 Loyalty Islands, New Caledonia. Tectonophysics, 709, 20-38.
741 Kanamori, H. (1972). Mechanism of tsunami earthquakes. Physics of the earth and planetary
742 interiors, 6(5), 346-359.
743 Lawson, C. L., & Hanson, R. J. (1995). Solving least squares problems. Society for Industrial
744 and Applied Mathematics.
745 Liu PLF, Woo SB, Cho YS. 1998. Computer programs for tsunami propagation and inundation.
746 New York (NY): Cornell University. Technical Report.
747 Lorito, S., Piatanesi, A., Cannelli, V., Romano, F., & Melini, D. (2010). Kinematics and source
748 zone properties of the 2004 Sumatra- Andaman earthquake and tsunami: Nonlinear joint
749 inversion of tide gauge, satellite altimetry, and GPS data. *Journal of Geophysical Research:*
750 *Solid Earth*, *115*(B2).
751 Lynnes, C. S., & Lay, T. (1988). Source process of the great 1977 Sumba earthquake. Journal
752 of Geophysical Research: Solid Earth, 93(B11), 13407-13420.

753 Matias, L., Baptista, M.A., Omira, R., Annunziato, A., Franchello, G., Carrilho, F. (2012).
754 Third generation tsunami scenario matrix for the Portuguese Tsunami Early Warning
755 System. Proceedings of the 15 WCEE, Lisboa, Portugal,
756 https://core.ac.uk/download/pdf/38626266.pdf.
757 Melgar, D., Ruiz-Angulo, A., Garcia, E. S., Manea, M., Manea, V. C., Xu, X., ... & Ramirez-
758 Guzmán, L. (2018). Deep embrittlement and complete rupture of the lithosphere during the
759 M w 8.2 Tehuantepec earthquake. Nature Geoscience, 11(12), 955-960.
760 Mulia, I. E., Gusman, A. R., & Satake, K. (2018). Alternative to non-linear model for
761 simulating tsunami inundation in real-time. Geophysical Journal International, 214(3),
762 2002-2013.
763 Mulia, I. E., Gusman, A. R., & Satake, K. (2020). Applying a deep learning algorithm to
764 tsunami inundation database of megathrust earthquakes. Journal of Geophysical Research:
765 Solid Earth, 125(9), e2020JB019690.
766 National Emergency Management Agency [NEMA]. 2020. Tsunami advisory and warning
767 plan: supporting plan [SP 01/20]. Wellington (NZ): National Emergency Management
768 Agency; [accessed 2020 Aug 10].
769 https://www.civildefence.govt.nz/assets/Uploads/publications-/Supporting-Plans/Tsunami-
770 Advisory-and-Warning-Plan-Supporting-Plan-Update-Jun-2020.pdf
771 Neil, H., Orpin, A., Nodder, S., MItchell, J., Northcote, L., Mackay, K., Kane, T. (2015). Large
772 Canyon-Channel Complexes from South Island of New Zealand Show Contrasting
773 Morphologies. AAPG Asia Pacific Region, Geoscience Technology Workshop, Modern
774 Depositional Systems as Analogues for Petroleum Reservoirs, April 21-22, 2015,
775 Wellington, New Zealand.
776 https://www.searchanddiscovery.com/abstracts/pdf/2015/90235gtw/abstracts/ndx_neil.pdf

777 Onat, Y., Yalciner, A.C. (2013). Initial stage of database development for tsunami warning
778 system along Turkish coasts. Ocean Engineering, 74, 141-154,
779 https://doi.org/10.1016/j.oceaneng.2013.09.008.
780 Okada, Y. (1985). Surface deformation due to shear and tensile faults in a half-space. Bulletin
781 of the seismological society of America, 75(4), 1135-1154.
782 Okal, E. A. (1988). Seismic parameters controlling far-field tsunami amplitudes: A review.
783 Natural Hazards, 1(1), 67-96.
784 Power, W., Wallace, L., Wang, X., & Reyners, M. (2012). Tsunami hazard posed to New
785 Zealand by the Kermadec and southern New Hebrides subduction margins: an assessment
786 based on plate boundary kinematics, interseismic coupling, and historical seismicity. Pure
787 and applied geophysics, 169(1), 1-36.
788 Power, W.L. (2017). A tool for Rapid Tsunami Threat (RTTM) generation. Lower Hutt, N.Z.:
789 GNS Science. *GNS Science report 2017/37.* 30 p.; doi: 10.21420/G2463J
790 Power, W.L.; Fry, B.; Gusman, A.R.; Burbidge, D.R.; Brewer, M.; Wang, X. 2018 DART
791 buoys network design. GNS Science consultancy report 2018/147. 53 p.
792 Reymond, D., Okal, E.A., Hébert, H., Bourdet, M. (2012). Rapid forecast of tsunami wave
793 heights from a database of pre- computed simulations, and application during the 2011
794 Tohoku tsunami in French Polynesia. Geophysical Research Letters, 39(11),
795 https://doi.org/10.1029/2012GL051640.
796 Roger, J., Pelletier, B. and Aucan, J. (2019). Update of the tsunami catalogue of New Caledonia
797 using a decision table based on seismic data and marigraphic records, Natural Hazards and
798 Earth System Sciences, 19, 1471-1483, https://doi.org/10.5194/nhess-19-1471-2019.
799 Roger, J., Pelletier, B., Duphil, M., Lefèvre, J., Aucan, J., Lebellegard, P., Thomas, B.,
800 Bachelier, C., Varillon, D. (2021). The Mw 7.5 Tadine (Maré, Loyalty Is.) earthquake and
801 related tsunami of December 5, 2018: implications for tsunami hazard assessment in New

802 Caledonia. Natural Hazards and Earth System Sciences, Discussions,
803 https://doi.org/10.5194/nhess-2021-58.
804 Romano, F., Piatanesi, A., Lorito, S., Tolomei, C., Atzori, S., & Murphy, S. (2016). Optimal
805 time alignment of tide- gauge tsunami waveforms in nonlinear inversions: Application to
806 the 2015 Illapel (Chile) earthquake. Geophysical Research Letters, 43(21), 11-226.
807 Rowden, A.A., Clark, M.R., Wright, I.C. (2005). Physical characterisation and a biologically
808 focused classification of "seamounts" in the New Zealand region. New Zealand Journal of
809 Marine and Freshwater Research, 2005, Vol. 39: 1039–1059. DOI:
810 10.1080/00288330.2005.9517374
811 Sahal A., Pelletier B., Chatelier J., Lavigne F. and Schindelé F.: A catalog of tsunamis in New
812 Caledonia from 28 March 1875 to 30 September 2009, Comptes Rendus Geoscience, 342,
813 437-444, 2010.
814 Satake, K. (1995). Linear and nonlinear computations of the 1992 Nicaragua earthquake
815 tsunami. Pure and Applied Geophysics, 144(3), 455-470.
816 Shepard, D. (1968, January). A two-dimensional interpolation function for irregularly-spaced
817 data. In Proceedings of the 1968 23rd ACM national conference (pp. 517-524).
818 Tanioka, Y., & Sataka, K. (1996). Fault parameters of the 1896 Sanriku tsunami earthquake
819 estimated from tsunami numerical modeling. *Geophysical Research Letters*, *23*(13), 1549-
820 1552.
821 Tanioka, Y., Miranda, G. J. A., Gusman, A. R., & Fujii, Y. (2017). Method to determine
822 appropriate source models of large earthquakes including tsunami earthquakes for tsunami
823 early warning in Central America. *Pure and applied geophysics*, *174*(8), 3237-3248.
824 Tatehata, H. (1997). The new tsunami warning system of the Japan Meteorological Agency.
825 In *Perspectives on Tsunami Hazard Reduction* (pp. 175-188). Springer, Dordrecht.

826 Titov, V.V., Moore, C.W., Greenslade, D.J.M. *et al.* A New Tool for Inundation Modeling:
827 Community Modeling Interface for Tsunamis (ComMIT). *Pure Appl. Geophys.* **168,** 2121–
828 2131 (2011). https://doi.org/10.1007/s00024-011-0292-4
829 Uruski, C. I. (2010). New Zealand's deepwater frontier. Marine and Petroleum Geology, 27(9),
830 2005-2026.
831 USGS, (2021). https://earthquake.usgs.gov/earthquakes/eventpage/us6000dg77/executive
832 Watada, S., Kusumoto, S., & Satake, K. (2014). Traveltime delay and initial phase reversal of
833 distant tsunamis coupled with the self- gravitating elastic Earth. Journal of Geophysical
834 Research: Solid Earth, 119(5), 4287-4310.
835 Wang X, Liu PLF. 2006. An analysis of 2004 Sumatra earthquake fault plane mechanisms and
836 Indian Ocean tsunami. Journal of Hydraulic Research. 44(2):147–154.
837 doi:10.1080/00221686.2006.9521671.
838 Wang X, Power WL. 2011. COMCOT: a tsunami generation, propagation and run-up model.
839 Lower Hutt (NZ): GNS Science. 121 p. (GNS Science report; 2011/43).
840 Wang, Y., Maeda, T., Satake, K., Heidarzadeh, M., Su, H., Sheehan, A. F., & Gusman, A. R.
841 (2019). Tsunami data assimilation without a dense observation network. Geophysical
842 Research Letters, 46(4), 2045-2053.
843 Yabuki, T., & Matsu'Ura, M. (1992). Geodetic data inversion using a Bayesian information
844 criterion for spatial distribution of fault slip. Geophysical Journal International, 109(2), 363-
845 375.
846
847